

Journal of Materials Chemistry B

Materials for biology and medicine

Accepted Manuscript

This article can be cited before page numbers have been issued, to do this please use: J. Huang, J. Huang, X. Ning, W. Luo, M. Chen, Z. Wang, W. Zhang, Z. Zhang and J. Chao, *J. Mater. Chem. B*, 2020, DOI: 10.1039/C9TB02652E.



This is an Accepted Manuscript, which has been through the Royal Society of Chemistry peer review process and has been accepted for publication.

Accepted Manuscripts are published online shortly after acceptance, before technical editing, formatting and proof reading. Using this free service, authors can make their results available to the community, in citable form, before we publish the edited article. We will replace this Accepted Manuscript with the edited and formatted Advance Article as soon as it is available.

You can find more information about Accepted Manuscripts in the [Information for Authors](#).

Please note that technical editing may introduce minor changes to the text and/or graphics, which may alter content. The journal's standard [Terms & Conditions](#) and the [Ethical guidelines](#) still apply. In no event shall the Royal Society of Chemistry be held responsible for any errors or omissions in this Accepted Manuscript or any consequences arising from the use of any information it contains.

ARTICLE

CT/NIRF dual-modal imaging tracking and therapeutic efficacy of transplanted mesenchymal stem cells labeled with Au nanoparticles in silica-induced pulmonary fibrosis

Received 00th January 20xx,
Accepted 00th January 20xx

DOI: 10.1039/x0xx00000x

Jie Huang^a, Jie Huang^b, Xinyu Ning^b, Wei Luo^{a,c,d}, Mengling Chen^{a,c,d}, Zhangyan Wang^{a,c,d}, Wei Zhang^{a,c,d}, Zhijun Zhang^{b*}, Jie Chao^{a,c,d,e*}

Abstract Mesenchymal stem cells (MSCs) have shown promising therapeutic effects in cell-based therapies and regenerative medicine. Efficient tracking of MSCs is an urgent clinical need that will help to understand their behavior after transplantation and allow adjustment of therapeutic strategies. However, no clinically approved tracers are currently available, which limits the clinical translation of stem cell therapy. In the current study, a nanoparticle (NP) for computed tomography (CT)/fluorescence dual-modal imaging, Au@Albumin@ICG@PLL (AA@ICG@PLL), was developed to track bone marrow-derived mesenchymal stem cells (BMSCs) administered intratracheally into mice with silica-induced pulmonary fibrosis, which facilitated understanding of the therapeutic effect and the possible molecular mechanism of stem cell therapy. The AuNPs have firstly formed in the bovine serum albumin (BSA) solution and modified with indocyanine green (ICG), subsequently coated the poly-L-lysine (PLL) layer to enhance intracellular uptake and biocompatibility. BMSCs were labeled with AA@ICG@PLL NPs with high efficiency without an effect on biological function or therapeutic capacity. The injected AA@ICG@PLL-labeled BMSCs could be tracked via CT and near-infrared fluorescence (NIRF) imaging for up to 21 days after transplantation. Using these NPs, the molecular anti-inflammatory mechanism of transplanted BMSCs was revealed, which included the downregulation of proinflammatory cytokines, suppression of macrophage activation, and delay of the fibrosis process. The current study suggests a promising role for imaging-guided MSC-based therapy for pulmonary fibrosis, such as idiopathic pulmonary fibrosis (IPF) and pneumoconiosis.

Keywords Mesenchymal stem cells; Au nanoparticles; CT/NIRF imaging tracking; Cell therapy; Silicosis

1. Introduction

Pulmonary fibrosis (PF) is a consequence of multiple interacting genetic and environmental risk factors and is regarded as an irreversible step in many pulmonary diseases, such as idiopathic pulmonary fibrosis (IPF) and pneumoconiosis (parenchymal lung disease arising from the inhalation of inorganic dust at work)¹⁻⁴. The most common, fastest-growing, and most serious type of pneumoconiosis is silicosis, which is caused by the inhalation of free crystalline silicon dioxide and is the occupational health issue with the highest incidence in developing countries⁵. Currently, available management strategies are focused on controlling the associated symptoms

and complications; there is no proven curative treatment for silicosis².

Recently, an increasing number of studies have elucidated the repair mechanisms and protective effects of MSCs in animal models of lung diseases⁶, including COPD⁷, ALI/ARDS⁸, IPF⁹ and silicosis¹⁰. MSCs are multipotent adult cells that can be isolated from various organs, including bone marrow, skin, umbilical cord, and adipose tissue. BMSCs are the most frequently studied MSCs¹¹. The strong immunosuppressive ability and low immunoreactivity of these cells make them safe for transplantation as autografts or allografts. Furthermore, their differentiation ability and paracrine effects make them valuable in tissue repair and regeneration. Some studies showed that BMSCs administration could inhibit proinflammatory and profibrotic cytokine release and relieve pathological changes associated with silica-induced PF in animal models^{10, 12}.

Although studies have recognized BMSC-based therapy as a new potential treatment option for silicosis, longitudinal, noninvasive methods to trace the cells post-transplantation and to evaluate their biodistribution, function, and final fate are lacking¹³. A clear understanding of the *in vivo* behavior of the transplanted cells will be not only helpful in determining the possible mechanism of stem cell therapy but also necessary for translation from basic research to clinical practice.

To date, biomedical imaging techniques, such as magnetic resonance imaging (MRI)¹⁴, CT imaging¹⁵, optical imaging¹⁶,

^a Department of Physiology, School of Medicine, Southeast University, Nanjing, Jiangsu, 210009, China.

^b CAS Key Laboratory of Nano-Bio Interface, Division of Nanobiomedicine, Suzhou Institute of Nano-Tech and Nano-Bionics, Chinese Academy of Sciences, Suzhou, Jiangsu, 215123, China.

^c Department of Respiration, Zhongda Hospital, School of Medicine, Southeast University, Nanjing, Jiangsu, 210009, China

^d Key Laboratory of Environmental Medicine Engineering, Ministry of Education, School of Public Health, Southeast University, Nanjing, Jiangsu, 210009, China

^e School of Medicine, Xizang Minzu University, Xianyang, Shanxi, 712082, China

* Corresponding authors: Zhijun Zhang, Ph.D., and Jie Chao, Ph.D.

Zhijun Zhang Email: zjzhang2007@sinano.ac.cn Tel: 86-512-62872556

Jie Chao Email: chaojie@seu.edu.cn Tel: +86-25-83272312

Electronic Supplementary Information (ESI) available: [details of any supplementary information available should be included here]. See DOI: 10.1039/x0xx00000x

single-photon emission tomography/positron emission tomography (SPECT/PET)¹⁷, and fluorescent imaging¹⁸, have been widely used for noninvasive cell tracking. Among these techniques, fluorescence is the most commonly used technique in small animal experiments investigating biological processes¹⁹. Cells labeled with specific reporter genes, such as green fluorescent protein (GFP) and luciferase, via viral vectors can be directly tracked in space and time by sensitive optical detectors. However, the use of viral vectors requires genetic modification, which affects the biological character of the cells to some extent. Alternatively, indocyanine green (ICG), a near-infrared fluorescence (NIRF) dye approved by the U.S. Food and Drug Administration (FDA) as a clinical imaging agent, has proven to be a promising clinical agent for effective and safe cell tracking in many diseases^{20, 21}. Furthermore, cells could be labeled with NPs, such as superparamagnetic iron oxide (SPIO) NPs²², Au NPs²³, and UCNPs²⁴, that enter the cell by endocytosis and then are trapped intracellularly to achieve cell tracking. Among these NPs, SPIO NPs have been applied for the visualization of MSCs via MRI in many disease models. Another class of inorganic NPs, gold NPs, can be detected by CT, a technique that provides higher spatial resolution than MRI. In the clinic, CT imaging is commonly used to image patients with suspected lung fibrosis due to its superior spatial resolution, fast acquisition time, moderate cost, and multiplanar capabilities²⁵. As each imaging method has its strengths and limitations, a combination of high spatial distribution CT with high-resolution NIRF could facilitate the evaluation of fibrosis and the tracking of stem cells.

In this work, we developed a novel CT/NIRF dual-modal imaging NP, AA@ICG@PLL, by conjugating Au@Albumin (AA) with ICG using albumin as a nanoreactor and poly-L-lysine (PLL) as a cationic transfection agent for visualization of transplanted BMSCs during the treatment of silica-induced lung fibrosis. AA@ICG@PLL NPs were effectively taken up by BMSCs before transplantation without affecting cell viability or differentiation ability. Moreover, by highly sensitive CT and fluorescence imaging of AA@ICG@PLL NPs, we imaged and traced labeled BMSCs for up to 21 d post-transplantation. We further demonstrated that the transplanted BMSCs played an anti-inflammatory role by inhibiting macrophage activation and exerted anti-fibrotic effects in a silica-induced lung fibrosis mouse model.

2. Results

2.1 Preparation and characterization of AA@ICG@PLL NPs

2.1.1 Synthesis of AA@ICG@PLL NPs:

Considering clinical convenience and affordability, NPs were designed based on the Au@Albumin NPs that were reported by Shi et al.²⁶. The synthesis process for AA@ICG@PLL NPs is shown in Figure 1A. $\text{HAuCl}_4 \cdot 3\text{H}_2\text{O}$ was reduced by $\text{N}_2\text{H}_4 \cdot \text{H}_2\text{O}$ in the BSA solution, which is used as a stabilizing agent to enhance the aqueous solubility, colloidal stability, and biocompatibility of AuNPs, followed by the formation of Au@Albumin NPs. Then, the NIRF dye ICG was loaded onto the

Au@Albumin NPs via electrostatic adsorption to generate Au@Albumin@ICG (AA@ICG) NPs. To improve the nanoparticle internalization, a positively charged transfection agent, PLL was then modified on the surface of AA@ICG NPs by physisorption as described in our previous study²⁷, thereby generating AA@ICG@PLL NPs.

2.1.2 Characterization of AA@ICG@PLL NPs:

The morphology and size of the prepared AA@ICG@PLL were characterized by transmission electron microscopy (TEM). Figure 1B showed that the NPs were spherical, with a diameter of $12.2 \text{ nm} \pm 1.59 \text{ nm}$, and had high dispersibility. The ultraviolet (UV)-visible (Vis) absorption spectra for Au@Albumin NPs, free ICG, AA@ICG, and AA@ICG@PLL NPs in water are presented in Figure 1C. Compared with Au@Albumin NPs, both AA@ICG and AA@ICG@PLL NPs showed the characteristic peak of ICG, and the absorption peaks of ICG on their surfaces were red-shifted compared to that of free ICG, which may be caused by physicochemical changes in ICG upon binding to protein²⁸ or aggregation²⁹, consistent with previous reports^{30, 31}. The amount of loaded ICG was not significantly different between AA@ICG NPs and AA@ICG@PLL NPs; the loading capacity reached approximately 27% (Figure 1D). The optical properties of the AA@ICG@PLL NPs were also detected. Measurement of the fluorescence spectra showed that the emission peak of ICG, when loaded in AA@ICG@PLL, was red-shifted by approximately 15 nm compared with free ICG and was still in the detection range (Figure S1A). The above results indicated that ICG successfully coated the surface of Au@Albumin NPs, and the PLL coating did not influence the ICG loading efficiency and the optical properties.

Then, the surface charge property and hydrodynamic size of the NPs were analyzed. The AA@ICG@PLL NPs had a positive zeta potential at approximately +35.1 mV, higher than that of AA@ICG (+4.1 mV), which facilitated the uptake of AA@ICG@PLL NPs by stem cells (Figures 1E, S1B)³². Figure 1F showed that the average hydrodynamic diameter of AA@ICG NPs tested by dynamic light scattering (DLS) was 43.5 nm. After the PLL coating, the size of the AA@ICG@PLL NPs increased to 59.3 nm but maintained a narrow size distribution, which was slightly larger than that observed by TEM due to the morphology of hydrated materials. The AA@ICG@PLL NPs showed limited variation (<20%) in hydrodynamic size after seven days of storage in deionized water at 4°C, indicating excellent stability in aqueous medium (Figure S1C). At the last time point of seven days' absorption spectra measurement, AA@ICG@PLL NPs showed a reduction in absorption intensity by approximately 19%, while the absorption value of free ICG had decreased dramatically by 63% (Figure S1D). These results showed that AA@ICG@PLL improved the absorption stability of free ICG and acted as an efficient carrier to deliver ICG to BMSCs for imaging function.

To check imaging ability, CT imaging of AA@ICG@PLL NPs diluted in ddH₂O was performed with a Hiscan XM Micro-CT (Suzhou Hiscan Information Technology Co., Ltd.). With increasing Au concentration, AA@ICG@PLL NPs gradually yielded brighter CT signals. The Hounsfield unit (HU) of

AA@ICG@PLL NPs was linearly dependent on the Au concentration (Figure 1G). Also, AA@ICG@PLL NPs had a higher attenuation coefficient than the clinically used CT contrast agent Iohexol, indicating the good CT imaging contrast ability of the NPs. Moreover, fluorescence images of ICG in AA@ICG@PLL NPs were obtained with a Maestro *in Vivo* Imaging System (CRI Inc., USA), and the results showed that the fluorescence signal strength was directly proportional to the Au concentration (Figure S2).

2.2 BMSCs labeled with AA@ICG@PLL NPs

To clarify the effect of BMSCs on lung tissue repair, a sensitive and reliable method of labeling BMSCs and tracking them *in vivo* is required. The capacity of BMSCs to uptake NPs has been confirmed in many studies³³. In order to determine the optimal conditions for cell labeling with AA@ICG@PLL NPs, dynamic processes of BMSCs uptake of NPs under different treatment times and concentrations were observed using a live cell imaging system. Figure 2A and Supplementary Movie 1 show that the accumulation of AA@ICG@PLL NPs gradually increased over time in whole cells. Considering the reduced BMSCs viability in the serum-free culture medium, 24h was chosen as the appropriate incubation time. The cell labeling efficiency at various Au concentrations (0, 50, 100, 200, and 300 $\mu\text{g mL}^{-1}$) was also observed under bright-field microscopy. As indicated in Figures 2B and S3A, the relative NP labeling area in the cytoplasm was concentration-dependent. The results of flow cytometry analysis shown in Figure S3B further confirmed that BMSCs were nearly 100% labeled after incubation for 24 h with AA@ICG@PLL NPs at an Au concentration of 200 $\mu\text{g mL}^{-1}$, then the intracellular Au content measured by inductively coupled plasma mass spectrometry (ICP-MS) was approximately 218 pg per cell (Figure 2C). Moreover, the CCK8 cell viability assays (Figure 2D) showed no significant alterations in cytotoxicity for concentrations up to 200 $\mu\text{g mL}^{-1}$. Based on the efficiency and toxicity results, the Au concentration 200 $\mu\text{g mL}^{-1}$ was chosen in the following experiments. To further confirm that the NPs were internalized by BMSCs, fluorescence confocal microscopy was used to image DiO and AA@ICG@PLL double-labeled BMSCs. The images in Figure 2E showed that AA@ICG@PLL NPs were trapped into the cytoplasm but not be attached to the surface.

Next, CT and NIRF imaging of the labeled BMSCs were performed *in vitro*. Compared to unlabeled BMSCs, labeled BMSCs exhibited stronger signals by CT imaging (Figure 2F); the average CT values were 84.4, 147.2, and 156 HU for BMSCs labeled with AA@ICG@PLL NPs at Au concentrations of 50, 100, and 200 $\mu\text{g mL}^{-1}$, respectively (Figure S4A). Fluorescence images of tubes containing labeled BMSCs with various Au concentrations were obtained; the labeled cells appeared high-intensity signals, whereas the unlabeled cells could not detect significant signals (Figure 2G). The total radiant efficiency of each tube containing AA@ICG@PLL NPs at Au concentrations of 50, 100, and 200 $\mu\text{g mL}^{-1}$ was calculated as 6.03×10^6 , 9.66×10^6 , and 1.36×10^7 photons/s/cm²/sr, respectively, demonstrating that the imaging signal of labeled BMSCs is Au concentration-

dependent (Figure S4B). These data illustrated the high sensitivity of CT and NIR detection *in vitro*, ensuring the reliability of labeled BMSC tracking in animals.

2.3 Effects of AA@ICG@PLL labeling on cell migration, differentiation, and proliferation

To evaluate the safety of AA@ICG@PLL labeling, cell migration, and proliferation were examined after labeling. As shown in Figure 3A and supplementary movie S2, most of the cells migrated from the initial location during the observation period. Cell division could also be observed during this period, (red arrows), indicating that the vitality of BMSCs was not affected by NPs. Furthermore, cultures of labeled BMSCs were expanded to further determine the fate of NPs in the cells (Figure 3B). BMSCs labeled with AA@ICG@PLL grew well after four passages in normal culture conditions. However, along with cellular proliferation, NP release by exocytosis was observed. At passage 4 (P4), after labeling, fewer than 50% of the NPs remained in the cytoplasm (Figure 3C).

To identify AA@ICG@PLL labeling would affect the differentiation capabilities of BMSCs or not, cells were first incubated with AA@ICG@PLL NPs labeling medium (200 $\mu\text{g mL}^{-1}$, 24h), and then changed to adipogenic or osteogenic induction medium. Osteoblasts secrete alkaline phosphatase (ALP), which likely degrades inorganic pyrophosphate to provide sufficient local phosphate for mineralization; therefore, ALP activity is commonly considered a marker of osteogenesis³⁴. As shown in Figure 3D and 3E, both labeled and unlabeled BMSCs exhibited purple NBT-formazan, which was produced by the reaction between ALP and BCIP/NBT. Regarding adipogenic differentiation, Oil Red O-stained lipid deposits were not different between labeled and unlabeled BMSCs. In short, the differentiation capabilities were not affected by AA@ICG@PLL NP labeling.

2.4 *In vivo* tracking of transplanted BMSCs during silica-induced PF

After determining the usability and safety of NPs *in vitro*, the feasibility of *in vivo* tracking of BMSCs in the silica-induced PF mouse model was investigated. The protocol is shown in Figure 4A, in which AA@ICG@PLL-labeled BMSCs (1×10^6 cells) suspended in 100 μL of saline were intratracheally transplanted into the lung, followed by CT and NIRF scanning. As shown in Figure 4B, CT images of mouse lungs from the labeled BMSC groups at day 7 (d7) post-transplantation indicated obvious CT signals. Moreover, a strong fluorescence signal from the ICG distributed in the lungs was detected by the Maestro *In Vivo* Imaging System (Figure 4C). Then, the mice were sacrificed, and *ex vivo* fluorescence intensity images of major organs, including the heart, lungs, liver, spleen, and kidneys, were obtained. As shown in Figure 4C, the fluorescence signal intensity was significantly higher in the lungs than in the other organs, which agreed with the above *in vivo* results. To more accurately and reliably track AA@ICG@PLL-labeled BMSCs *in vivo*, the cell membrane dye DiO was used to mark BMSCs before transplantation. At 7 d post-transplantation, signals from DiO

(green) and ICG (red) showed co-localization in mouse lung tissue slide analysis (Figure 4D).

As BMSC therapy is expected to play a role in both the early inflammation and in late fibrosis stages, the feasibility of continuous *in vivo* tracking of labeled BMSCs in the silica-induced PF mouse model was explored. Figure 5A shows the CT images at 7 d, 14 d, and 21 d after labeled BMSCs transplantation, while the image obtained pre-transplantation was used as a control. Compared to the control group, CT signals of the labeled BMSCs could be tracked up to 21 d in the right lung after transplantation (square box in Figure 5A and 5B). Moreover, the NIRF images in Figure 5C revealed that strong fluorescence signals could also be observed for 21 d in the lung after transplantation. Fluorescence from double-labeled BMSCs detected in lung tissue slides at different time points confirmed the signals captured by CT and NIRF scanning (Figure 5D). These results demonstrated that AA@ICG@PLL-labeled BMSCs could be monitored for up to 21 d after transplantation.

2.5 BMSCs ameliorate silica-induced lung fibrosis

To confirm the safety and usability of labeled BMSCs in a clinical setting, experimental silicosis mouse models were generated³⁵. The technical scheme of this experiment is shown in Figure 6A. The mice were treated with AA@ICG@PLL-labeled or unlabeled BMSCs (1×10^6) intratracheally on d7 after exposure to a silica suspension. After CT imaging on d28, all mice were sacrificed for subsequent analyses.

First, the safety of labeled BMSC transplantation in a PF mouse model was evaluated. As shown in Figure 6B, there was no significant difference in mouse body weight among groups, and no mice died during the experimental period. Hematoxylin and eosin (H&E) staining of heart, liver, spleen, and kidney tissues (Figure 6C) showed no obvious changes among groups. In the lungs, the alveolar structure was markedly destroyed in the SiO₂ group compared to the control group, accompanied by a large area of inflammatory cell aggregation. After the transplantation of BMSCs, the alveolar damage was decreased, and inflammatory cell aggregation was weaker, while no difference in the therapeutic effect was observed between labeled and unlabeled BMSCs. These results suggested that BMSC transplantation in silica-induced PF mouse models was safe and that labeled BMSCs could maintain their treatment effects.

To further evaluate the clinical application of labeled BMSCs, CT imaging, histopathology, and plasma hydroxyproline assays were performed. Figure 7A shows representative images of radiological features in the lungs of mice in each group at d28. The lungs of mice in the control group were clear. However, different-sized high-density or reticular fibrous shadows and signs of traction bronchiectasis were found to be diffusely distributed in the lungs of mice in the SiO₂ group. In the labeled and unlabeled BMSC transplantation groups, the typical radiological features of an inflammatory response and the fibrotic changes were alleviated. Sirius red staining of collagen deposition (Figure 7B) revealed increased extracellular matrix deposition in lung sections from mice exposed to silica

compared with those in the control group. Collagen deposition and associated fibrosis were alleviated after labeled or unlabeled BMSC transplantation. In addition to the histopathology analysis, plasma hydroxyproline content, a marker of collagen deposition, and overall degree of fibrosis, was also assessed (Figure S5). After labeled or unlabeled BMSC transplantation, the plasma hydroxyproline content was quantifiably reduced compared to SiO₂ treatment alone. These results suggested NPs did not affect the antifibrotic role of BMSCs in a silica-induced PF mouse model.

2.6 BMSCs exert a protective effect by downregulating macrophage activation in silica-induced PF

Silicosis is initiated via the phagocytosis of silica particles by alveolar macrophages; these activated macrophages release various oxidants and cytokines, which play crucial roles both in the early inflammation and late fibrosis stages of the disease³⁶. The active inflammatory response is characterized by neutrophil and macrophage infiltration of the interstitium and alveolar spaces after silica exposure. First, HE staining of lung tissue (Figures 6C and S6A) demonstrated that BMSC transplantation could alleviate lung inflammation and reduce cell infiltration in silica-induced lung injury. Many studies, including our previous studies^{37,38}, have shown the vital roles of macrophages in silicosis, especially in inflammation during disease progression. Therefore, we examined the expression of F4/80, a macrophage marker, in lung tissue from the above groups and observed significantly increased F4/80 expression in the SiO₂ group compared with the control group (Figure S6B). However, the high F4/80 expression level was decreased after BMSC treatment, suggesting that BMSC treatment could reduce the number of macrophages in silica-induced lung injury. Moreover, proinflammatory cytokines secreted by macrophages, such as TNF- α , IL-6, and CXCL2, were detected in lung tissue and BALF by RT-PCR and ELISA. As shown in Figure 7C, BMSCs ameliorated the severity of lung inflammation by downregulating the mRNA levels of these proinflammatory cytokines in lung tissue. Similar results of attenuated TNF- α , IL-6, and CXCL2 protein levels upon BMSC transplantation were found in the BALF analysis (Figure 7D). These results indicated that BMSC administration ameliorated silica-induced lung injury by attenuating lung inflammation via the downregulation of proinflammatory cytokine and chemokine expression and production.

To determine whether labeled BMSCs share the same molecular mechanism of silica-induced macrophage activation with normal BMSCs, *in vitro* experiments involving THP-1-derived macrophages were performed. Consistent with previous data³⁹, Figures S7A-B show the silica-induced activation of THP-1-derived macrophages, characterized by the significant time-dependent increases in the protein levels of NOS2 (M1 macrophage marker) and ARG and SOCS3 (M2 macrophage markers) after SiO₂ exposure. Then, THP-1-derived macrophages exposed to SiO₂ exposure for 24 h were treated with BMSC conditioned medium (CM). As shown in Figures 8A-B, BMSC-CM significantly suppressed the SiO₂-induced

expression of markers of macrophage activation compared to the control medium, and the effects were concentration-dependent. We also collected conditioned medium from labeled BMSCs, which had similar therapeutic effects as that from control BMSCs, suggesting that AA@ICG@PLL labeling does not influence the therapeutic potential of BMSCs (Figures 8C-D). This finding was confirmed by immunocytochemistry (Figure 8E).

3. Discussion

Even though therapeutic strategies based on stem cell transplantation have shown great potential in experimental lung injury models^{40, 41}, there is limited information about the fate of BMSCs after transplantation into the lungs. In a previous study, Xu et al. used highly sensitive *in vivo* upconversion luminescence (UCL) imaging^{13, 42} in acute lung injury mouse models to show that human amniotic fluid-derived stem (hAFS) cells labeled with UCNP-PEG-PEI migrated to the lungs over 72 h. Sean V. Murphy et al. tried to use a gadolinium-based Trimetasphere®-positive contrast agent to track hAFS cells via MRI¹⁴, and the labeled cells could be tracked within lung tissue for up to one week after transplantation. With the demand for more accurate information on transplanted cells, some studies have tried to combine two or more imaging modalities to trace cells^{43, 44}. In this study, we successfully prepared novel AA@ICG@PLL NPs to perform dual CT and NIRF imaging tracking of labeled BMSCs for up to 21 d post-transplantation in a PF mouse model.

Due to the high contrast between air-filled lungs and soft tissues, CT imaging can provide detailed 3D structural information at high spatial and temporal resolution and thus is more suitable than other methods for cell tracking in lung disease models. Among various CT contrast agents, Au NPs have the largest atomic number and X-ray absorption coefficient, straightforward surface modifiability, and good biocompatibility^{13, 15, 42}. However, Au NPs cannot be detected directly on tissue slides, while the commercially available tracking reagent SPIO can be visualized by Prussian blue staining. To achieve efficient and reliable cell tracking signals, it is necessary to combine the strengths of different imaging modalities. Because of their super-high sensitivity, real-time mod, and high contrast, optical imaging techniques are widely used in disease examination and therapy⁴⁵⁻⁴⁸. Light in the near-infrared region of approximately 700–900 nm, which can maximize tissue penetrance in addition to minimizing the autofluorescence from nontarget tissue, is ideal for imaging deeper tissues⁴⁹. Furthermore, NIRF signals can be detected by confocal microscopy *ex vivo* in tissues to confirm the reliability of signals *in vivo*. In previous studies, several NIRF nanoprobes have been used for cell tracking, such as cy5.5, quantum dots (QD), and ICG. Though QD was used to track stem cells transplanted into the liver⁵⁰ and brain⁵¹, the risk of pro-thrombosis mediated by QD labeling of cells was reported firstly in 2010 by Ramot Y⁵². Therefore, in this study, AuNPs were modified with ICG, a NIRF dye currently used in several clinical imaging applications^{21, 53} with attractive, stable optical

absorption; the resulting NPs could be detected by *in vivo* NIRF imaging and *in vitro* confocal imaging. DOI: 10.1039/C9TB02652E

Cell tracking NPs must meet several criteria in addition to image contrast ability. 1. High cell labeling efficiency. Uptake of sufficient NPs into each cell is necessary to achieve good detection of transplanted BMSCs. Therefore, in the process of synthesizing AA@ICG@PLL NPs, PLL was used to modify the surface of AA@ICG NPs by physisorption. This modification did not affect the physiochemical properties of the NPs but did promote highly efficient internalization into BMSCs, consistent with previous reports^{54, 55}. 2. Biological safety. *In vitro* and *in vivo* experiments confirmed that AA@ICG@PLL NP labeling does not affect cell viability or disrupt cell functions, such as migration, proliferation, and differentiation. Labeled cells maintained therapeutic effects and showed no adverse impacts on mouse body weight or major organs. 3. Long-range *in vivo* cell-tracking property. Referring to previous studies^{56, 57}, we transplanted 1×10^6 AA@ICG@PLL-labeled BMSCs intratracheally into mice with silica-induced PF. At 21 d post-transplantation, signals from labeled cells were still detectable in the mouse lungs via CT and NIRF, and the ICG fluorescence were colocalized with DiO-labeled BMSCs in lung tissue slides, demonstrating the presence of AA@ICG@PLL. Importantly, AA@ICG@PLL NPs were confirmed as suitable cell-tracking NPs with noninvasive and long-term tracing potential. However, there are still several problems that remain to be solved: NPs labelling BMSCs through endocytosis could also be removed or diluted during cell proliferation or apoptosis, then taken up by live BMSCs or macrophages as previously reported^{58, 59}; these processes could lead to signal attenuation and fluorescence quenching during the tracking process. Furthermore, the signals from NPs could not distinguish between live and dead cells. Potential ways to address these issues could be firstly modifying the NPs to extend the intracellular retention time without affecting the cell biological features, then combining cell-tracking NPs with reporter genes or finding specific CT signal characteristics that could represent the different conditions of the NPs. These ideas will be investigated in our future studies.

After monitoring the accumulation of AA@ICG@PLL-labeled BMSCs in PF mouse lungs, we further explored the therapeutic mechanism of these transplanted cells in PF models. Previous studies suggested that the effects of MSC-based silicosis treatment may result from the suppression of IL-1 signaling through IL1-Ra and a decrease in TNF- α expression⁶⁰ during early inflammation or from the inhibition of SiO₂-induced EndoMT through the regulation of ER stress and autophagy⁶¹ in late fibrosis. In this study, we focused on exploring the effects of MSCs on macrophages, which are essential for both inflammatory reactions and the development of fibrosis³⁸. When macrophages respond to external stimuli, such as SiO₂ exposure in this study, they functionally polarize into different phenotypes, specifically the classically activated (M1) and alternatively activated (M2) phenotypes⁶². Activated macrophages produce cytokines that provoke proliferative signaling by fibroblasts and ultimately induce alterations in collagen metabolism and deposition in the lungs. We found that BMSC transplantation could decrease the alveolar macrophage

population in mice with PF, and BMSC-CM could downregulate the markers related to macrophage activation, suggesting that paracrine secretion might be an essential mechanism by which BMSCs exert therapeutic effects. However, the specific cytokines involved and the underlying mechanism warrant further investigation.

4. Conclusion

Novel AA@ICG@PLL NPs suitable for CT/NIRF dual-modal imaging were synthesized and used to label and track BMSCs without interfering with cellular migration, proliferation, and differentiation. The labeled BMSCs could be tracked for up to 21 d after transplantation *in vivo* by NIRF and CT imaging, and the transplanted BMSCs downregulated silica-induced macrophage activation and played an anti-inflammatory and antifibrotic roles in the silica-induced PF mouse model. Our work may provide a potential way to achieve long-term tracking of transplanted BMSCs in the treatment of silicosis.

5. Experimental section

Reagents

HAuCl₄·3H₂O (520918) and PLL (MW=30 kD, P1024) were purchased from Sigma-Aldrich. BSA and ICG were purchased from BBI Life Sciences Co. SiO₂ with a diameter of approximately 2–5 μm was purchased from Sigma (S5631). The silica was sterilized overnight (200°C for 16 h) and then diluted in sterile NS to 5 mg/mL or 50 mg/mL for *in vitro* or *in vivo* experiments. Rabbit polyclonal antibody to NOS2 (18985-1-AP) was obtained from Proteintech (Rosemont, IL, USA), and ARG1 (9819S) and SOCS-3 (2923S) antibodies were obtained from Cell Signaling Technology (Danvers, MA, USA). An anti-F4/80 antibody (ab100790) was purchased from Abcam (Cambridge, MA, USA). Mouse TNFα, IL-6, and CXCL2 ELISA kits were obtained from Proteintech.

Cell culture

Human BMSCs isolated from bone marrow aspirates were purchased from Nanjing Drum Tower Clinical Stem Cell Center and cultured as previously described. The cells were cultured in T75 flasks in DMEM/F12 containing 10% FBS, penicillin (100 U/mL), streptomycin (100 μg/mL), and 2 mM L-glutamine at 37°C in a 5% CO₂ atmosphere. The medium was changed every three days. BMSCs at P3-8 were used for all experiments. Adipogenic and osteogenic differentiation media purchased from Cyagen Biosciences were used according to the manufacturer's instructions.

The human monocytic cell line THP-1 (ATCC) was cultured in RPMI 1640 medium containing 10% FBS, streptomycin (100 μg/mL), and penicillin (100 U/mL) in a 5% CO₂ atmosphere at 37°C. Then, 50 nM phorbol myristate acetate (PMA) was used to stimulate 6×10⁵ THP-1 cell per well differentiation for 24 h before the experiments.

AA@ICG@PLL NP synthesis and characterization

The synthetic process of Au@Albumin NPs was similar to that described previously, with moderate modifications. Briefly, 500 mg BSA was dissolved in 20 mL deionized water, then added HAuCl₄·3H₂O (9.2 mL, 25.39 mM). After 5-10 min stirring, N₂H₄·H₂O (40 μL) was added into the mixture, and continuously stirred for 30 min. After the intensive mixing, the unreacted BSA and N₂H₄·H₂O were removed through dialysis for 6 h to get the purified product, Au@Albumin NPs. The surface of NPs was coated with the NIRF dye ICG by adding Au@Albumin into 5 mL of a 1 mg/mL ICG solution and then stirring for 12 h. Free ICG was removed via ultrafiltration to get AA@ICG NPs. Lastly, PLL and AA@ICG NPs at a mass ratio of 3:200 were mixed and sonicated for 3 h, yielding the AA@ICG@PLL nanotracer.

The TEM images of AA@ICG@PLL were conducted using the transmission electron microscope operating at an accelerating voltage of 100 kV. UV-Vis spectra were obtained using a Shimadzu UV2550 UV-Vis spectrophotometer. The ICG loading capacity was calculated with the following equation: loading efficiency = $W_{\text{ICG}}/W_{\text{Au}} \times 100\%$, where W_{ICG} represents the weight of ICG loaded on NPs, and W_{Au} represents the weight of Au in NPs. The hydrodynamic diameter and size distribution, as well as the zeta potential, were determined by the ZEN3600 Nano ZS instrument (Malvern). The emission spectra were detected by a fluorescence spectrometer (FluoroMax-4 Compact Spectrofluorometer, HORIBA Scientific) with excitation of 760 nm, and the emission spectra were recorded from 770 to 850 nm. Both the excitation slit width and emission slit width were 5 nm. ICP-MS (Thermo Fisher Scientific) was used to determine the intracellular Au concentration.

Cell loading with AA@ICG@PLL NPs

AA@ICG@PLL NPs resuspended in serum-free medium were added in excess to BMSCs at 37°C for 24 h. After incubation, the cells were washed twice with PBS to remove unbound NPs and collected for subsequent experiments.

Cell viability assessments

CCK8 assays were performed to evaluate BMSC viability after labeling with AA@ICG@PLL NPs. CCK8 reagent (5 mg/mL, Sigma-Aldrich) was added to each well, and the cells were incubated at 37°C for 1-4 h. The colored solution was transferred to a 96-well plate, and the resulting absorbance was read at 550 nm.

Animal experiments

All animals were maintained on a 12:12 h light/dark cycle under constant temperature (23°C) and humidity (50%) conditions with free access to food and water. All animal procedures were approved by the Laboratory Animal Care and Use Committee at Southeast University and were performed in strict accordance with the National Institutes of Health Guide for the Care and Use of Laboratory Animals.

Male C57BL/6 mice were divided into four groups (n≥6 each group), the control, SiO₂, SiO₂+BMSC, and SiO₂+labeled BMSC groups. After anesthesia induced by pentobarbital sodium (1%, 50 mg/kg), mice were intratracheally administered 100 μL of a

silica suspension, except for those in the control group, which received 100 μL of saline. Then, the mice in the control and SiO_2 groups were intratracheally injected with 100 μL of saline, and those in the SiO_2 +BMSC and SiO_2 -labeled BMSC groups received 100 μL of BMSCs (1×10^6) or AA@ICG@PLL-labeled BMSCs (1×10^6), respectively, on d7 following the intratracheal administration of silica.

CT imaging

CT imaging in this study was captured by a micro-CT system (Hiscan XM) followed these scanning parameters: voltage, 60 kV; electricity, 133 μA ; scanning resolution, 50 μm ; single exposure time, 1.2 s; scanning circle, 360°; scanning angle interval, 0.5°. The reconstruction and analysis software programs were provided by Hiscan.

NIR fluorescence imaging

In vitro and *in vivo* NIR fluorescence images of ICG (704 nm excitation and 735 nm filter) were obtained with a Maestro *in Vivo* Imaging System (CRI Inc., USA).

Histopathological examination

Mice were sacrificed, and the organs were quickly isolated, fixed in 4% paraformaldehyde, embedded in OCT and cut into 5-mm-thick sections. Tissues on glass slides were stained with H&E for histopathological evaluation and with Sirius red for fibrosis assessments following the manufacturer's directions.

Real-time fluorescent quantitative RT-PCR

The relative mRNA expression of TNF- α , IL-6, and CXCL2 in lung tissue was determined by RT-PCR. Mouse primers used in this study were purchased from Invitrogen, and the sequences were provided in Table S1.

ELISA

For detection of TNF- α , IL-6, and CXCL2 level in mice BALF. 1mL BALF collected from each mouse was centrifuged at $300 \times g$ for 5 min at 4 °C, and the supernatant collected for cytokine analysis by ELISA following the manufacturer's directions. Blood samples for hydroxyproline level analysis were collected from mice in different groups. After centrifuging at $3000 \times g$ for 15 min at 4 °C, the plasma was used for ELISA following the manufacturer's directions.

Western blotting

The expression levels of specific proteins in THP-1-derived macrophages were determined by Western blotting, as previously described³⁵. Briefly, the treated cells were lysed to get total protein. The protein concentration was quantified through BCA, according to the manufacturer's instructions. Equal amounts of the proteins in different groups were separated via SDS-PAGE gel electrophoresis and transferred to PVDF membranes. After blocking, the membranes were incubated with specific primary antibodies at 4°C overnight and then with secondary antibodies for 1 h at room temperature.

The protein amounts loaded were normalized according to the GAPDH signal.

DOI: 10.1039/C9TB02652E

Immunofluorescence

The cell and tissue Immunofluorescence were performed as previously described³⁹. Briefly, the treated cells and lung tissues were fixed with 4% paraformaldehyde for 15 min at room temperature, followed by permeabilization with 0.3% Triton X-100. After that, 10% normal goat serum was added to block for 2 h at room temperature and then incubated with specific primary antibodies at 4°C overnight. Finally, the appropriate fluorescent secondary antibodies were added at a 1:400 dilution for 2 h and the nuclei were stained with DAPI.

Statistical analysis

The data are presented as the mean \pm SEM. Unpaired numerical data were compared using an unpaired t-test (two groups) or analysis of variance (ANOVA; more than two groups). A p-value of <0.05 was considered to indicate statistical significance.

Conflicts of interest

There are no conflicts to declare.

Acknowledgements

This study is the result of work that was partially supported by resources and facilities at the Core Laboratory at the Medical School of Southeast University. This work was supported by the National Key R&D Program of China (2017YFA0104303 and 2017YFA0104301) and The National Natural Science Foundation of China (nos. 81773796 and 81972987).

References

1. L. Richeldi, H. R. Collard and M. G. Jones, *Lancet*, 2017, **389**, 1941-1952.
2. C. C. Leung, I. T. S. Yu and W. Chen, *The Lancet*, 2012, **379**, 2008-2018.
3. N. Fujimura, *Curr Opin Pulm Med*, 2000, **6**, 140-144.
4. P. Cullinan and P. Reid, *Prim Care Respir J*, 2013, **22**, 249-252.
5. M. Lopes-Pacheco, E. Bandeira and M. M. Morales, *Stem Cells International*, 2016, **2016**, 1-9.
6. S. Geiger, D. Hirsch and F. G. Hermann, *Eur Respir Rev*, 2017, **26**.
7. X. Li, C. Michaeloudes, Y. Zhang, C. H. Wiegman, I. M. Adcock, Q. Lian, J. C. W. Mak, P. K. Bhavsar and K. F. Chung, *J Allergy Clin Immunol*, 2018, **141**, 1634-1645 e1635.
8. X. Fang, J. Abbott, L. Cheng, J. K. Colby, J. W. Lee, B. D. Levy and M. A. Matthay, *J Immunol*, 2015, **195**, 875-881.
9. R. L. Toonkel, J. M. Hare, M. A. Matthay and M. K. Glassberg, *Am J Respir Crit Care Med*, 2013, **188**, 133-

- 140.
10. E. Zhang, Y. Yang, S. Chen, C. Peng, M. F. Lavin, A. J. Yeo, C. Li, X. Liu, Y. Guan, X. Du, Z. Du and H. Shao, *Stem Cell Res Ther*, 2018, **9**, 311.
 11. R. L. Heise, P. A. Link and L. Farkas, *Front Pediatr*, 2016, **4**, 80.
 12. X. Li, Y. Wang, G. An, D. Liang, Z. Zhu, X. Lian, P. Niu, C. Guo and L. Tian, *Toxicol Lett*, 2017, **270**, 96-107.
 13. O. Betzer, A. Schwartz, M. Motiei, G. Kazimirsky, I. Gispán, E. Damti, C. Brodie, G. Yadid and R. Popovtzer, *ACS Nano*, 2014, **8**, 9274-9285.
 14. S. V. Murphy, A. Hale, T. Reid, J. Olson, A. Kidiyoor, J. Tan, Z. Zhou, J. Jackson and A. Atala, *Methods*, 2016, **99**, 99-111.
 15. J. Kim, P. Chhour, J. Hsu, H. I. Litt, V. A. Ferrari, R. Popovtzer and D. P. Cormode, *Bioconjug Chem*, 2017, **28**, 1581-1597.
 16. J. Li, W. Y. Lee, T. Wu, J. Xu, K. Zhang, G. Li, J. Xia and L. Bian, *Adv Healthc Mater*, 2016, **5**, 1049-1057.
 17. L. Bindslev, M. Haack-Sorensen, K. Bisgaard, L. Kragh, S. Mortensen, B. Hesse, A. Kjaer and J. Kastrup, *Eur J Nucl Med Mol Imaging*, 2006, **33**, 1171-1177.
 18. E. J. Oh, H. W. Lee, S. Kalimuthu, T. J. Kim, H. M. Kim, S. H. Baek, L. Zhu, J. M. Oh, S. H. Son, H. Y. Chung and B. C. Ahn, *J Control Release*, 2018, **279**, 79-88.
 19. J. C. Kim, J. L. Lee, Y. S. Yoon, A. M. Alotaibi and J. Kim, *Int J Med Robot*, 2016, **12**, 710-717.
 20. G. Wang, F. Zhang, R. Tian, L. Zhang, G. Fu, L. Yang and L. Zhu, *ACS Appl Mater Interfaces*, 2016, **8**, 5608-5617.
 21. L. Boni, G. David, A. Mangano, G. Dionigi, S. Rausei, S. Spampatti, E. Cassinotti and A. Fingerhut, *Surg Endosc*, 2015, **29**, 2046-2055.
 22. C. A. Bourzac, J. B. Koenig, K. A. Link, S. G. Nykamp and T. G. Koch, *Am J Vet Res*, 2014, **75**, 1010-1017.
 23. P. Nold, R. Hartmann, N. Feliu, K. Kantner, M. Gamal, B. Pelaz, J. Huhn, X. Sun, P. Jungebluth, P. Del Pino, H. Hackstein, P. Macchiarini, W. J. Parak and C. Brendel, *J Nanobiotechnology*, 2017, **15**, 24.
 24. Y. Xu, J. Xiang, H. Zhao, H. Liang, J. Huang, Y. Li, J. Pan, H. Zhou, X. Zhang, J. H. Wang, Z. Liu and J. Wang, *Biomaterials*, 2016, **100**, 91-100.
 25. E. Hammond, J. D. Newell, Jr., S. K. Dilger, N. Stoyles, J. Morgan, J. P. Sieren, D. R. Thedens, E. A. Hoffman, D. K. Meyerholz and J. C. Sieren, *Toxicol Pathol*, 2016, **44**, 373-381.
 26. H. Shi, Z. Wang, C. Huang, X. Gu, T. Jia, A. Zhang, Z. Wu, L. Zhu, X. Luo, X. Zhao, N. Jia and F. Miao, *Small*, 2016, **12**, 3995-4006.
 27. X. Ning, H. Bao, X. Liu, H. Fu, W. Wang, J. Huang and Z. Zhang, *Nanoscale*, 2019, **11**, 20932-20941.
 28. T. Desmettre, J. M. Devoisselle and S. Mordon, *Surv Ophthalmol*, 2000, **45**, 15-27.
 29. M. Maurer, A. Penzkofer and J. Zweck, *J Photoch Photobio B*, 1998, **47**, 68-73.
 30. B. S. Jung and B. Anvari, *Biotechnol Progr*, 2012, **28**, 533-539.
 31. S. J. Song, S. He, Y. Tao, L. Wang, F. Han, H. B. Chen and Z. J. Zhang, *Acs Appl Mater Inter*, 2017, **9**, 9484-9495.
 32. T. Kim, N. Lee, D. R. Arifin, I. Shats, M. Janowski, P. Walczak, T. Hyeon and J. W. M. Bulte, *Advanced Functional Materials*, 2017, **27**.
 33. A. Ariza de Schellenberger, H. Kratz, T. D. Farr, N. Iowa, R. Hauptmann, S. Wagner, M. Taupitz, J. Schnorr and E. A. Schellenberger, *Int J Nanomedicine*, 2016, **11**, 1517-1535.
 34. L. Huang, P. Jin, X. Lin, C. Lin, L. Zheng and J. Zhao, *Mol Med Rep*, 2017, **15**, 1149-1156.
 35. Z. Zhou, R. Jiang, X. Yang, H. Guo, S. Fang, Y. Zhang, Y. Cheng, J. Wang, H. Yao and J. Chao, *Theranostics*, 2018, **8**, 575-592.
 36. D. Vanhee, P. Gosset, A. Boitelle, B. Wallaert and A. B. Tonnel, *Eur Respir J*, 1995, **8**, 834-842.
 37. H. Liu, Y. Cheng, J. Yang, W. Wang, S. Fang, W. Zhang, B. Han, Z. Zhou, H. Yao, J. Chao and H. Liao, *Cell Death Dis*, 2017, **8**, e2657.
 38. H. Liu, S. Fang, W. Wang, Y. Cheng, Y. Zhang, H. Liao, H. Yao and J. Chao, *Part Fibre Toxicol*, 2016, **13**, 55.
 39. X. Yang, J. Wang, Z. Zhou, R. Jiang, J. Huang, L. Chen, Z. Cao, H. Chu, B. Han, Y. Cheng and J. Chao, *FASEB J*, 2018, **32**, 3264-3277.
 40. X. Li, S. Yue and Z. Luo, *Oncotarget*, 2017, DOI: 10.18632/oncotarget.18126.
 41. N. H. Nicolay, R. Lopez Perez, J. Debus and P. E. Huber, *Cancer Lett*, 2015, **366**, 133-140.
 42. P. A. Jackson, W. N. Rahman, C. J. Wong, T. Ackerly and M. Geso, *Eur J Radiol*, 2010, **75**, 104-109.
 43. Y. Tang, C. Zhang, J. Wang, X. Lin, L. Zhang, Y. Yang, Y. Wang, Z. Zhang, J. W. Bulte and G. Y. Yang, *Adv Funct Mater*, 2015, **25**, 1024-1034.
 44. M. Lu, X. Cheng, J. Jiang, T. Li, Z. Zhang, C. Tsauo, Y. Liu and Z. Wang, *PLoS One*, 2018, **13**, e0193362.
 45. C. Chen, X. Ni, S. Jia, Y. Liang, X. Wu, D. Kong and D. Ding, *Adv Mater*, 2019, **31**, e1904914.
 46. C. Chen, H. Ou, R. Liu and D. Ding, *Adv Mater*, 2019, DOI: 10.1002/adma.201806331, e1806331.
 47. M. Li, Y. Ning, J. Chen, X. Duan, N. Song, D. Ding, X. Su and Z. Yu, *Nano Lett*, 2019, **19**, 7965-7976.
 48. T. Hara and F. A. Jaffer, *Curr Cardiovasc Imaging Rep*, 2016, **9**.
 49. A. Volpe, E. Kurtys and G. O. Fruhwirth, *Int J Biochem Cell Biol*, 2018, **102**, 40-50.
 50. H. Yukawa, M. Watanabe, N. Kaji, Y. Okamoto, M. Tokeshi, Y. Miyamoto, H. Noguchi, Y. Baba and S. Hayashi, *Biomaterials*, 2012, **33**, 2177-2186.
 51. Y. Zhu, H. Hong, Z. P. Xu, Z. Li and W. Cai, *Curr Mol Med*, 2013, **13**, 1549-1567.
 52. Y. Ramot, M. Steiner, V. Morad, S. Leibovitch, N. Amouyal, M. F. Cesta and A. Nyska, *Nanotoxicology*, 2010, **4**, 98-105.
 53. K. E. Wilson, S. V. Bachawal, L. Abou-Elkacem, K.

View Article Online

DOI: 10.1039/C9TB00535F

- Jensen, S. Machtaler, L. Tian and J. K. Willmann, *Theranostics*, 2017, **7**, 1463-1476.
54. S. Albukhaty, H. Naderi-Manesh and T. Tiraihi, *Iran Biomed J*, 2013, **17**, 71-76.
55. I. M. Pongrac, M. Dobrivojevic, L. B. Ahmed, M. Babic, M. Slouf, D. Horak and S. Gajovic, *Beilstein J Nanotechnol*, 2016, **7**, 926-936.
56. H. G. de Oliveira, F. F. Cruz, M. A. Antunes, A. V. de Macedo Neto, G. A. Oliveira, F. M. Svartman, T. Borgonovo, C. L. Rebelatto, D. J. Weiss, P. R. Brofman, M. M. Morales, E. S. J. R. Lapa and P. R. Rocco, *Stem Cells Transl Med*, 2017, **6**, 962-969.
57. D. J. Weiss, *Stem Cells*, 2014, **32**, 16-25.
58. A. K. Silva, C. Wilhelm, J. Kolosnjaj-Tabi, N. Luciani and F. Gazeau, *Pharm Res*, 2012, **29**, 1392-1403.
59. S. W. Kang, S. Lee, J. H. Na, H. I. Yoon, D. E. Lee, H. Koo, Y. W. Cho, S. H. Kim, S. Y. Jeong, I. C. Kwon, K. Choi and K. Kim, *Theranostics*, 2014, **4**, 420-431.
60. M. M. Zhao, J. Z. Cui, Y. Cui, R. Li, Y. X. Tian, S. X. Song, J. Zhang and J. L. Gao, *Mol Med Rep*, 2013, **8**, 741-746.
61. R. Jiang, Y. Liao, F. Yang, Y. Cheng, X. Dai and J. Chao, *Exp Cell Res*, 2019, DOI: 10.1016/j.yexcr.2019.07.005, 111492.
62. A. Sica and A. Mantovani, *J Clin Invest*, 2012, **122**, 787-795.

Figure Legend

Figure 1. Synthesis and characterization of AA@ICG@PLL NPs

A. Schematic illustration of the synthesis of AA@ICG@PLL NPs. **B.** The TEM image of AA@ICG@PLL NPs (inset shows the size distribution of AA@ICG@PLL NPs, $12.2 \text{ nm} \pm 1.594 \text{ nm}$). Scale bar=200 nm. **C.** UV-Vis absorption spectra of Au@Albumin NPs, free ICG, AA@ICG, and AA@ICG@PLL NPs in water. **D.** Loading efficiency of AA@ICG and AA@ICG@PLL NPs. **E.** Zeta potential measurements of AA@ICG and AA@ICG@PLL NPs. **F.** DLS data of AA@ICG and AA@ICG@PLL NPs in aqueous solution. **G.** Transverse CT images and calculated HU values of AA@ICG@PLL NPs and iohexol at different Au and I concentrations.

Figure 2. BMSCs labeled with AA@ICG@PLL NPs

A. Bright-field images of BMSCs incubated with AA@ICG@PLL NPs at 0 h, 6 h, 12 h, and 24 h. Scale bar=20 μm . **B.** Bright-field images of BMSCs incubated with AA@ICG@PLL NPs at various Au concentrations (0, 50, 100, 200, and 300 $\mu\text{g mL}^{-1}$) for 24 h. Scale bar=50 μm . **C.** Intracellular Au content measured by ICP-MS. **D.** Relative viability of BMSCs labeled with AA@ICG@PLL NPs at various Au concentrations. * $p < 0.05$ compared with the unlabeled group. **E.** Fluorescence confocal microscopy images of BMSCs labeled with AA@ICG@PLL NPs at 200 $\mu\text{g mL}^{-1}$ Au. The DiO-stained cell membrane (green), DAPI-stained cell nucleus (blue), ICG (red). Scale bar=20 μm . **F.** In vitro CT imaging of

agarose phantoms containing BMSCs labeled with different Au concentrations. **G.** In vitro NIRF images of agarose phantoms containing BMSCs labeled with different Au concentrations.

Figure 3. Effects of labeling on cell migration, differentiation, and proliferation

A. Time-lapse monitoring of AA@ICG@PLL-labeled BMSCs over a 24 h culture period revealed cell division (red arrow). Scale bar=50 μm . **B.** Images of BMSCs labeled with AA@ICG@PLL NPs after passaging from P1 to P4. Scale bar=20 μm . **C.** Column graph of the AA@ICG@PLL NP labeling area in BMSCs from P1 to P4. **D.** Bright-field images of Oil Red O staining and ALP staining of NP-loaded and unloaded BMSCs. Scale bar=20 μm . **E.** Column graph of the area positive for Oil Red O and ALP.

Figure 4. Tracking of AA@ICG@PLL-labeled BMSCs in a silica-induced PF mouse model

A. Experimental design for tracking AA@ICG@PLL-labeled BMSCs in a silica-induced PF mouse model. **B.** CT images of the lungs in model mice at 7 d after transplantation with or without AA@ICG@PLL-labeled BMSCs. **C.** In vivo NIRF images of the lungs in model mice at 7 d after transplantation with or without AA@ICG@PLL-labeled BMSCs. In vitro NIRF images of various organs at 7 d post-transplantation. **D.** Bright-field and immunofluorescence images of lung tissue slices in each group ($\text{SiO}_2 + \text{NS}$ and $\text{SiO}_2 + \text{labeled BMSCs}$) at 7 d post-transplantation. DiO (green), AA@ICG@PLL NPs (red), and DAPI-labeled nuclei (blue) are shown in the images. Scale bar=20 μm .

Figure 5. Long-term tracking of AA@ICG@PLL-labeled BMSCs

A. In vivo CT images of AA@ICG@PLL-labeled BMSCs at 7 d, 14 d, and 21 d after transplantation. An image of the lung before transplantation was used as a control. **B.** 3D CT images of labeled BMSCs at 21 d post-transplantation. An image of the lung before transplantation was used as a control. **C.** In vivo NIRF images of AA@ICG@PLL-labeled BMSCs at 7 d, 14 d, and 21 d after transplantation. An image of the lung before transplantation was used as a control. **D.** Immunofluorescence images of lung tissue slices collected at 7 d, 14 d, and 21 d after labeled BMSC transplantation. Scale bar=50 μm .

Figure 6. The safety of labeled BMSC transplantation in a PF mouse model

A. Study design for the following animal experiments. **B.** The body weight of mice in each group was measured every week during the experiment. **C.** H&E staining of essential organs (lungs, heart, liver, spleen, and kidneys). Scale bar=20 μm .

Figure 7. The effect of transplanted BMSCs on silica-induced lung fibrosis

A. CT examination of lungs from mice in each group on d28: Control, SiO₂+NS, SiO₂+BMSC, and SiO₂+labeled BMSC groups. **B.** Sirius red staining of lung sections from each group on d28: Control, SiO₂+NS, SiO₂+BMSC, and SiO₂+labeled BMSC groups. Scale bar=20 μm. **C.** mRNA levels of the inflammatory cytokines TNF-α, IL-6, and CXCL2 in the lungs from the Control, SiO₂+NS, SiO₂+BMSC, and SiO₂+labeled BMSC groups on d28 (n=6). ***p<0.001 compared with the control group. ##p<0.01, #p<0.05 compared with the SiO₂+NS group. **D.** Protein levels of the inflammatory cytokines TNF-α, IL-6, and CXCL2 in BALF from the Control, SiO₂+NS, SiO₂+BMSC, and SiO₂+labeled BMSC groups on d28 (n=6). *p<0.05 compared with the control group. #p<0.05 compared with the SiO₂+NS group.

View Article Online
DOI: 10.1039/C9TB02652E

Figure 8. Macrophage activation induced by SiO₂ exposure was suppressed after BMSC transplantation

A. Representative Western blot showing the effects of different concentrations of BMSC-CM on the expression of the macrophage activation markers NOS2, ARG1, and SOCS3 (L: 2.5x10⁴, M: 5x10⁴, and H: 1x10⁵). **B.** Densitometric analyses of Western blots from 3 separate experiments showing the effects of conditioned medium collected from different numbers of MSCs (L: 2.5x10⁴, M: 5x10⁴, and H: 1x10⁵) on SiO₂-induced macrophage activation. *p<0.05 vs. the control group; #p<0.05, ##p<0.01 vs. the SiO₂ group. **C.** Representative Western blot showing the effects of CM collected from unlabeled or labeled BMSCs on the expression of the macrophage activation markers NOS2, ARG1, and SOCS3. **D.** Densitometric analyses of Western blots from 3 separate experiments showing the effects of conditioned medium collected from labeled and unlabeled MSCs on SiO₂-induced macrophage activation. *p<0.05 vs. the control group; #p<0.05 vs. the SiO₂ group. **E.** Representative immunocytochemistry illustrating the ability of unlabeled or labeled BMSC-CM to downregulate macrophage activation. Scale bar=20 μm.

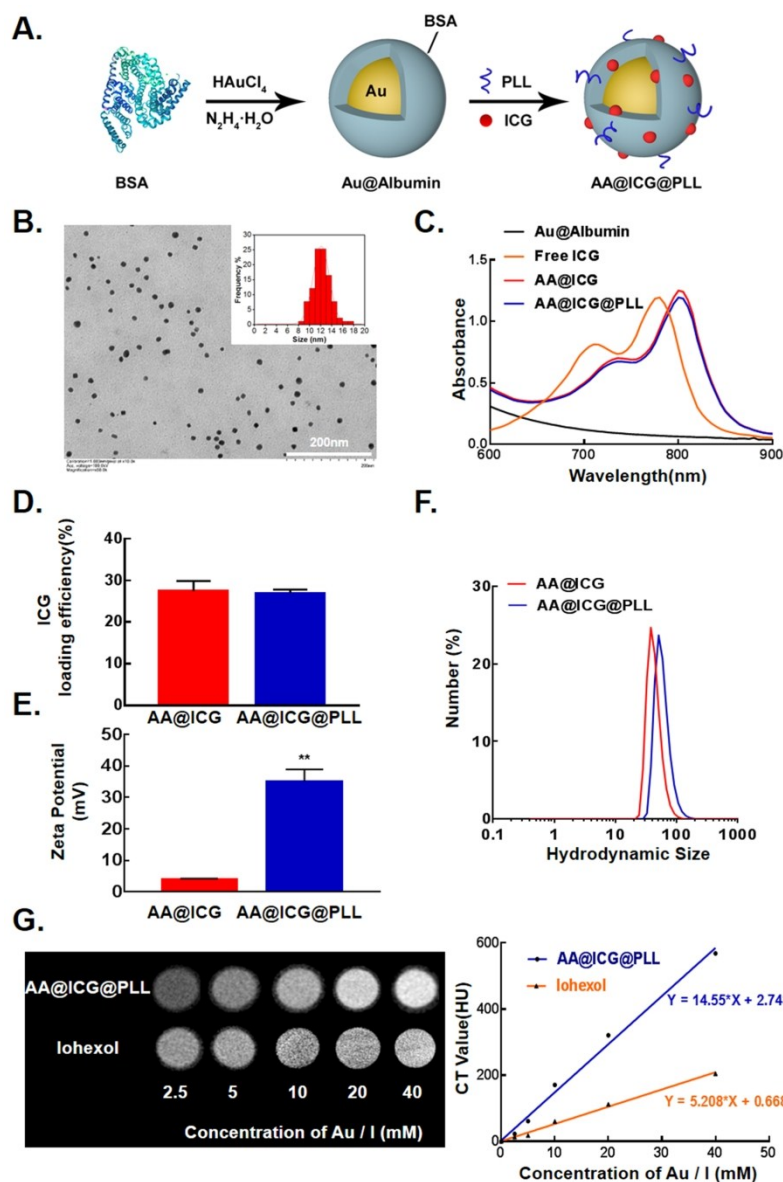


Figure 1. Synthesis and characterization of AA@ICG@PLL NPs

A. Schematic illustration of the synthesis of AA@ICG@PLL NPs. B. The TEM image of AA@ICG@PLL NPs (inset shows the size distribution of AA@ICG@PLL NPs, $12.2 \text{ nm} \pm 1.594 \text{ nm}$). Scale bar=200 nm. C. UV-Vis absorption spectra of Au@Albumin NPs, free ICG, AA@ICG, and AA@ICG@PLL NPs in water. D. Loading efficiency of AA@ICG and AA@ICG@PLL NPs. E. Zeta potential measurements of AA@ICG and AA@ICG@PLL NPs. F. DLS data of AA@ICG and AA@ICG@PLL NPs in aqueous solution. G. Transverse CT images and calculated HU values of AA@ICG@PLL NPs and iohexol at different Au and I concentrations.

155x233mm (300 x 300 DPI)

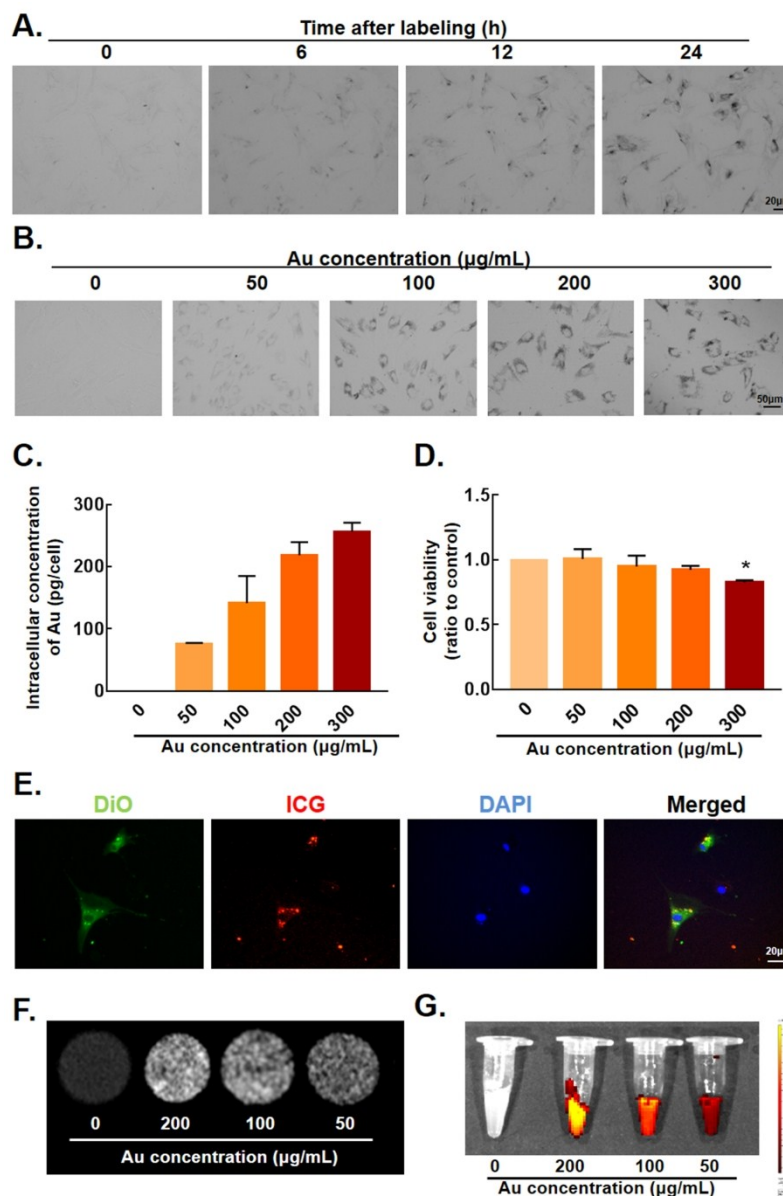


Figure 2. BMSCs labeled with AA@ICG@PLL NPs

A. Bright-field images of BMSCs incubated with AA@ICG@PLL NPs at 0 h, 6 h, 12 h, and 24 h. Scale bar=20 µm. B. Bright-field images of BMSCs incubated with AA@ICG@PLL NPs at various Au concentrations (0, 50, 100, 200, and 300 µg mL⁻¹) for 24 h. Scale bar=50 µm. C. Intracellular Au content measured by ICP-MS. D. Relative viability of BMSCs labeled with AA@ICG@PLL NPs at various Au concentrations. *p<0.05 compared with the unlabeled group. E. Fluorescence confocal microscopy images of BMSCs labeled with AA@ICG@PLL NPs at 200 µg mL⁻¹ Au. The DiO-stained cell membrane (green), DAPI-stained cell nucleus (blue), ICG (red). Scale bar=20 µm. F. In vitro CT imaging of agarose phantoms containing BMSCs labeled with different Au concentrations. G. In vitro NIRF images of agarose phantoms containing BMSCs labeled with different Au concentrations.

155x233mm (300 x 300 DPI)

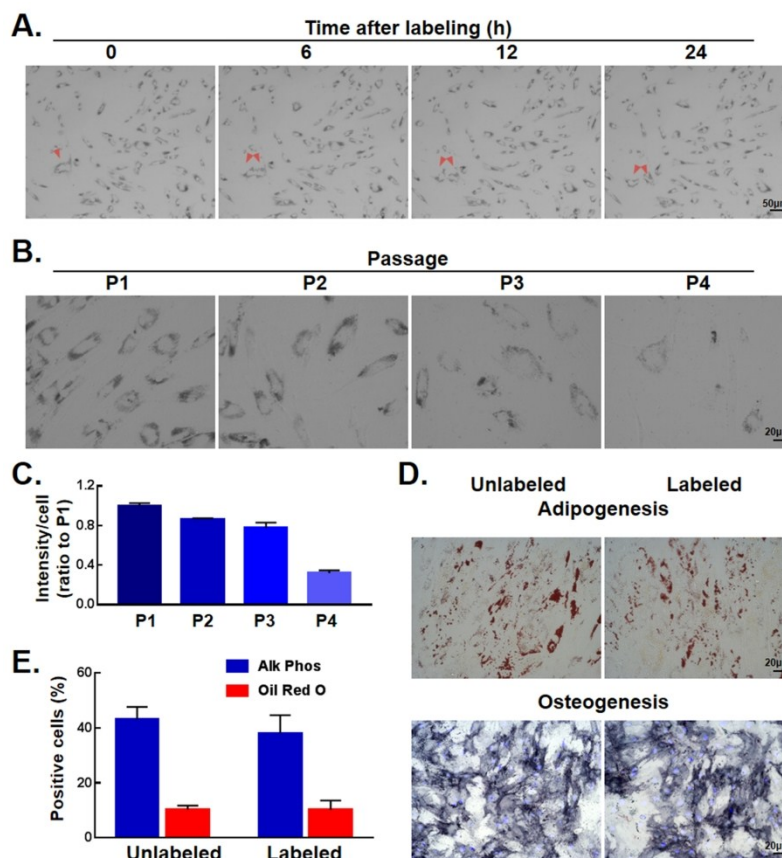


Figure 3. Effects of labeling on cell migration, differentiation, and proliferation

A. Time-lapse monitoring of AA@ICG@PLL-labeled BMSCs over a 24 h culture period revealed cell division (red arrow). Scale bar=50 μ m. B. Images of BMSCs labeled with AA@ICG@PLL NPs after passaging from P1 to P4. Scale bar=20 μ m. C. Column graph of the AA@ICG@PLL NP labeling area in BMSCs from P1 to P4. D. Bright-field images of Oil Red O staining and ALP staining of NP-loaded and unloaded BMSCs. Scale bar=20 μ m. E. Column graph of the area positive for Oil Red O and ALP.

155x233mm (300 x 300 DPI)

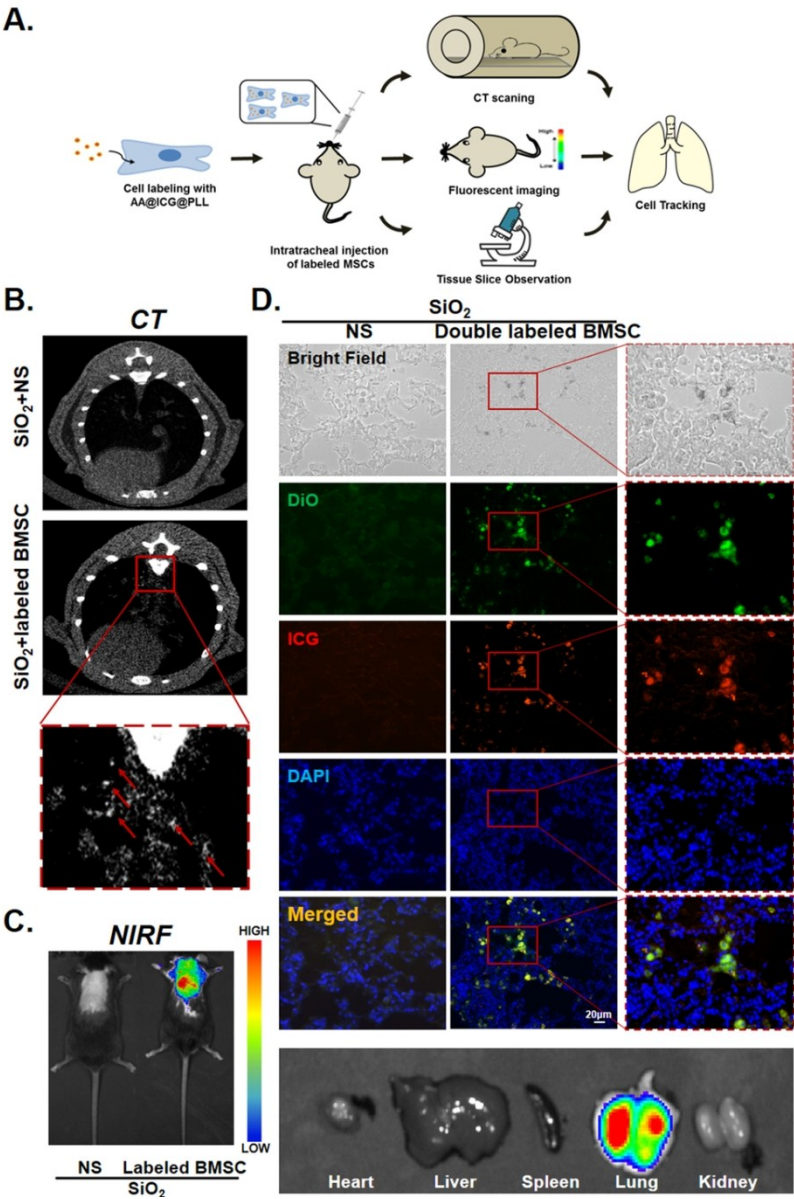


Figure 4. Tracking of AA@ICG@PLL-labeled BMSCs in a silica-induced PF mouse model
A. Experimental design for tracking AA@ICG@PLL-labeled BMSCs in a silica-induced PF mouse model. B. CT images of the lungs in model mice at 7 d after transplantation with or without AA@ICG@PLL-labeled BMSCs. C. In vivo NIRF images of the lungs in model mice at 7 d after transplantation with or without AA@ICG@PLL-labeled BMSCs. In vitro NIRF images of various organs at 7 d post-transplantation. D. Bright-field and immunofluorescence images of lung tissue slices in each group (SiO₂+NS and SiO₂+labeled BMSCs) at 7 d post-transplantation. DiO (green), AA@ICG@PLL NPs (red), and DAPI-labeled nuclei (blue) are shown in the images. Scale bar=20 μm.

82x124mm (300 x 300 DPI)

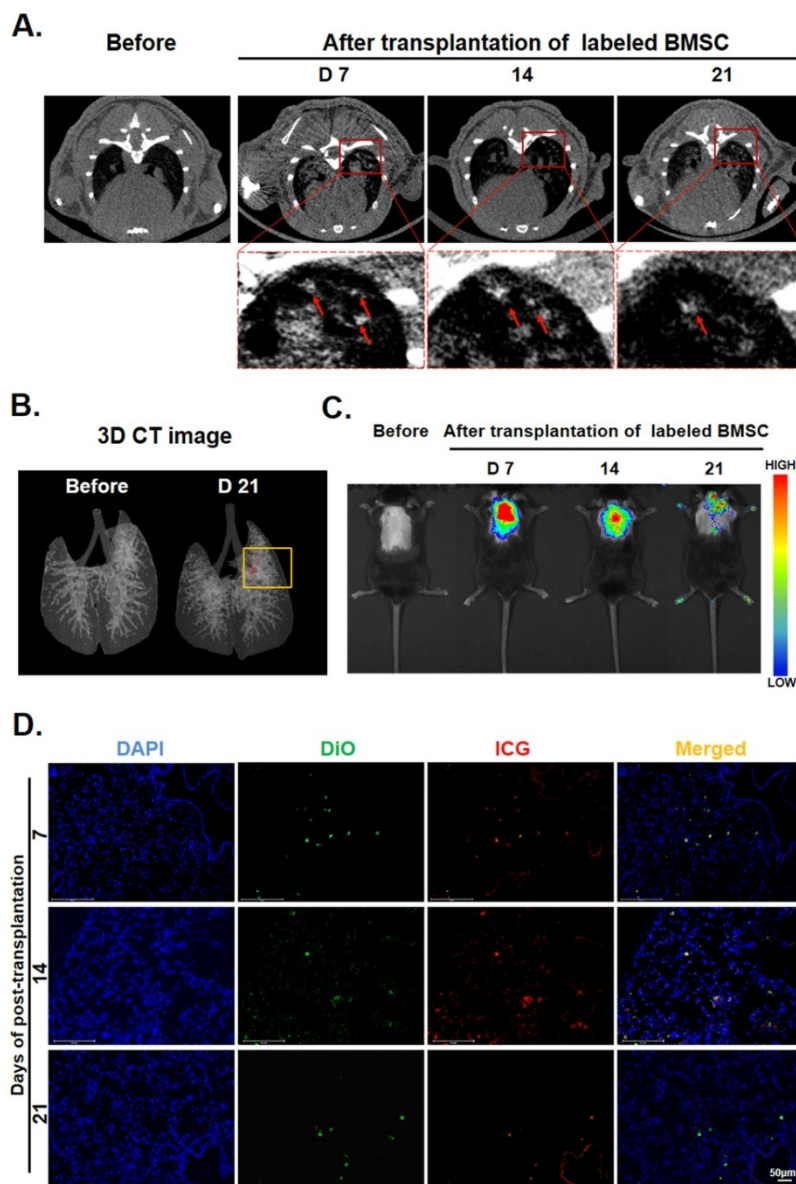


Figure 5. Long-term tracking of AA@ICG@PLL-labeled BMSCs

A. In vivo CT images of AA@ICG@PLL-labeled BMSCs at 7 d, 14 d, and 21 d after transplantation. An image of the lung before transplantation was used as a control. B. 3D CT images of labeled BMSCs at 21 d post-transplantation. An image of the lung before transplantation was used as a control. C. In vivo NIRF images of AA@ICG@PLL-labeled BMSCs at 7 d, 14 d, and 21 d after transplantation. An image of the lung before transplantation was used as a control. D. Immunofluorescence images of lung tissue slices collected at 7 d, 14 d, and 21 d after labeled BMSC transplantation. Scale bar=50 μ m.

82x124mm (300 x 300 DPI)

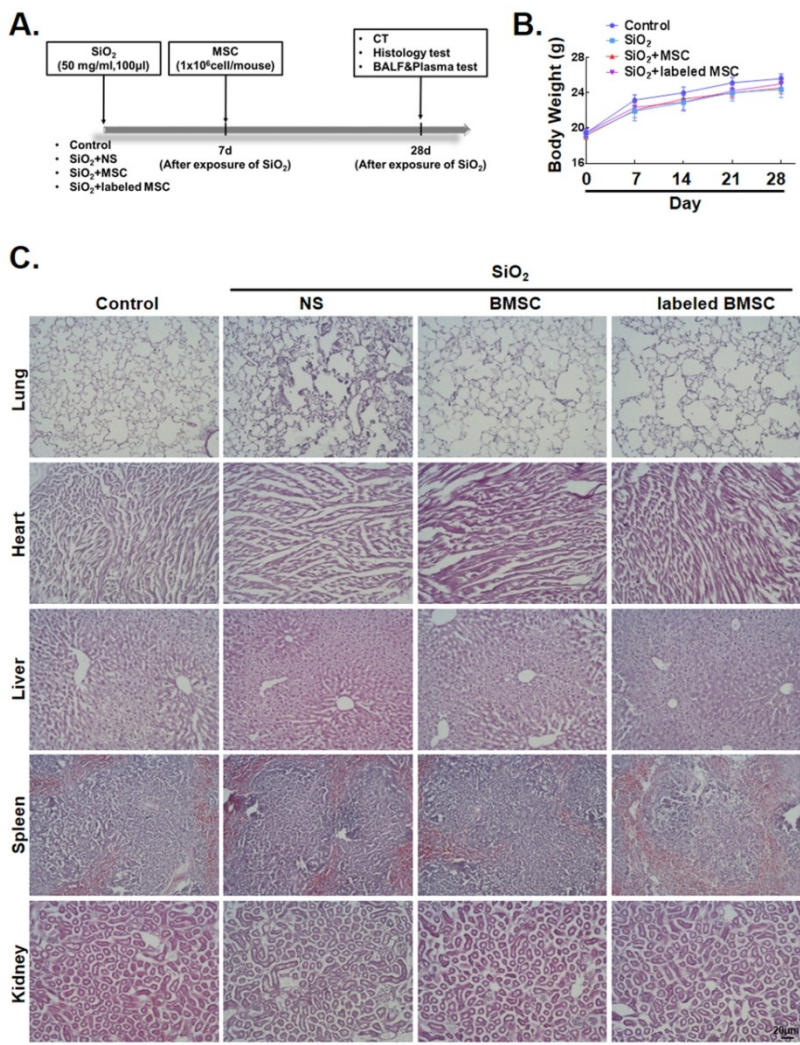


Figure 6. The safety of labeled BMSC transplantation in a PF mouse model
A. Study design for the following animal experiments. B. The body weight of mice in each group was measured every week during the experiment. C. H&E staining of essential organs (lungs, heart, liver, spleen, and kidneys). Scale bar=20 μm.

82x124mm (300 x 300 DPI)

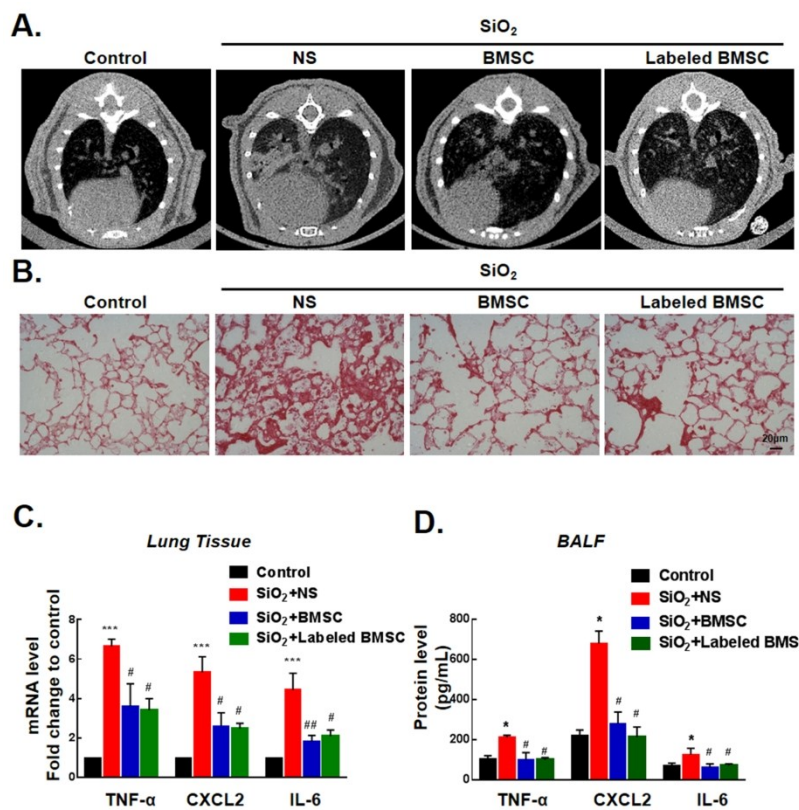


Figure 7. The effect of transplanted BMSCs on silica-induced lung fibrosis

A. CT examination of lungs from mice in each group on d28: Control, SiO₂+NS, SiO₂+BMSC, and SiO₂+labeled BMSC groups. B. Sirius red staining of lung sections from each group on d28: Control, SiO₂+NS, SiO₂+BMSC, and SiO₂+labeled BMSC groups. Scale bar=20 μm. C. mRNA levels of the inflammatory cytokines TNF-α, IL-6, and CXCL2 in the lungs from the Control, SiO₂+NS, SiO₂+BMSC, and SiO₂+labeled BMSC groups on d28 (n=6). ***p<0.001 compared with the control group. ##p<0.01, #p<0.05 compared with the SiO₂+NS group. D. Protein levels of the inflammatory cytokines TNF-α, IL-6, and CXCL2 in BALF from the Control, SiO₂+NS, SiO₂+BMSC, and SiO₂+labeled BMSC groups on d28 (n=6). *p<0.05 compared with the control group. #p<0.05 compared with the SiO₂+NS group.

155x233mm (300 x 300 DPI)

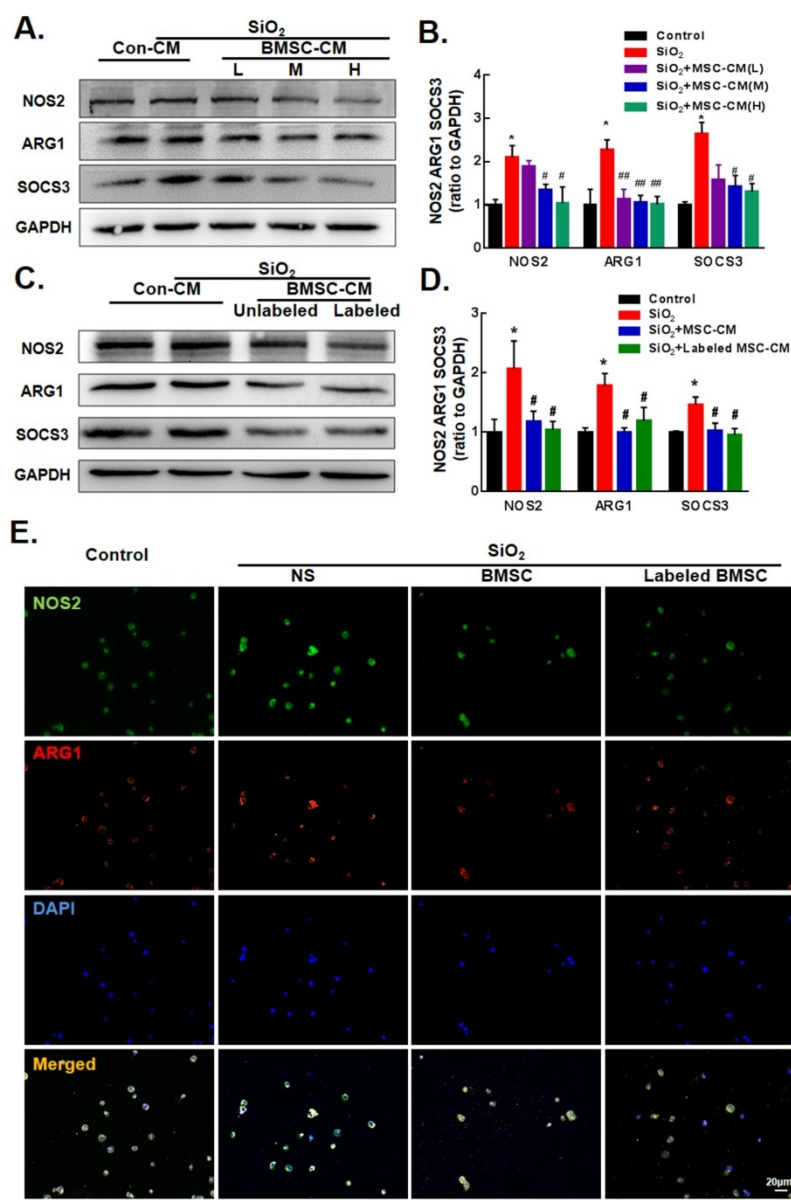
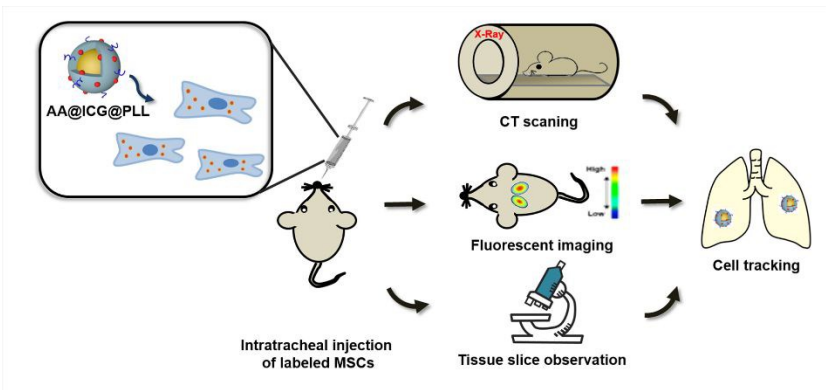


Figure 8. Macrophage activation induced by SiO₂ exposure was suppressed after BMSC transplantation

A. Representative Western blot showing the effects of different concentrations of BMSC-CM on the expression of the macrophage activation markers NOS2, ARG1, and SOCS3 (L: 2.5x10⁴, M: 5x10⁴, and H: 1x10⁵). B. Densitometric analyses of Western blots from 3 separate experiments showing the effects of conditioned medium collected from different numbers of MSCs (L: 2.5x10⁴, M: 5x10⁴, and H: 1x10⁵) on SiO₂-induced macrophage activation. *p<0.05 vs. the control group; #p<0.05, ##p<0.01 vs. the SiO₂ group. C. Representative Western blot showing the effects of CM collected from unlabeled or labeled BMSCs on the expression of the macrophage activation markers NOS2, ARG1, and SOCS3. D. Densitometric analyses of Western blots from 3 separate experiments showing the effects of conditioned medium collected from labeled and unlabeled MSCs on SiO₂-induced macrophage activation. *p<0.05 vs. the control group; #p<0.05 vs. the SiO₂ group. E. Representative immunocytochemistry illustrating the ability of unlabeled or labeled BMSC-CM to downregulate macrophage activation. Scale bar=20 μm.

155x233mm (300 x 300 DPI)



AA@ICG@PLL NPs, CT/NIRF dual model nanotracers, were synthesized to track BMSCs in the treatment of pulmonary fibrosis.